Plasma wake simulations and object charging in a shadowed lunar crater during a solar storm.

M. I. Zimmerman[1,2], T. L. Jackson[1,2], W. M. Farrell[1,2], T. J. Stubbs[1,2,3]

[1]NASA Goddard Space Flight Center, Greenbelt, MD, USA.

[2]NASA Lunar Science Institute, NASA Ames Research Center, Moffett Field, CA, USA.

[3]Center for Research and Exploration in Space Science and Technology, University of Maryland, Baltimore County, MD, USA.

michael.i.zimmerman@nasa.gov

Abstract

Within a permanently shadowed lunar crater the horizontal flow of solar wind is obstructed by upstream topography, forming a plasma wake that electrostatically diverts ions toward the crater floor and generates a surface potential that can reach kilovolts. In the present work kinetic plasma simulations are employed to investigate the morphology of a lunar crater wake during passage of a solar storm. Results are cast in terms of leading dimensionless ratios including the ion Mach number, ratio of crater depth to plasma Debye length, peak secondary electron yield, and electron temperature vs. electron impact energy at peak secondary yield. This small set of ratios allows generalization to a much wider range of scenarios. The kinetic simulation results are fed forward into an equivalent-circuit model of a roving astronaut. In very low-plasma-current environments triboelectric charging of the astronaut suit becomes effectively perpetual, representing a critical engineering concern for roving within shadowed lunar regions. Finally, simulated ion fluxes are used to explore sputtering and implantation processes within an idealized crater. It is suggested that the physics of plasma mini-wakes formed in the vicinity of permanently shadowed topography may play a critical role in modulating the enigmatic spatial distribution of volatiles at the lunar poles.

1. Introduction

From a human exploration perspective permanently shadowed lunar craters have the advantage of being thermally stable, potentially volatile-rich, [Paige et al. 2010] and in some locations providing nearby accessibility to steady sunlight as an

energy source. However, within a shadowed crater the direct flow of solar wind is obstructed by the upstream crater wall, forming a complicated plasma wake that modulates the particle fluxes and electrostatic environment far downstream [Zimmerman et al. 2011; Farrell et al. 2010]. Astronauts and robots venturing onto the crater floor will accumulate charge through direct exposure to spatially inhomogeneous plasma and secondary currents, and will undergo triboelectric charging due to frictional contact with the surface [Jackson et al. 2011]. These charging processes potentially represent an electrical discharge hazard to the astronaut suit as well as other infrastructure including sensitive instrumentation [Jackson et al. 2011]. Furthermore, the processes of ion implantation and sputtering are thought to play a role in the local balance of volatiles, which may someday be exploited to produce water and other useful compounds in situ [Shearer and Neal, 2011; Neal, 2009]. Understanding the environments within permanently shadowed regions (PSRs) of the Moon, under the wide variety of solar wind conditions experienced at 1 AU, will feed forward into future in situ mission planning and provides a unique laboratory for exploring the physics of plasma wakes.

The overarching goal of this work is to characterize the crater wake plasma environment, its effects on astronaut charging, and the volatile balance within an idealized polar crater during passage of a coronal mass ejection (CME). This is achieved by coupling a kinetic plasma model of wake structure [Zimmerman et al. 2011] with a numerical model of object charging [Jackson et al. 2010] and experimental and theoretical results on volatile sputtering [Johnson et al. 1989; cf. Killen et al. 2012 and references therein]. It will be shown that the coupled

wake/surface system is highly sensitive to fluctuations in solar wind conditions during the various stages of the passing CME, and the charge state of a roving astronaut will vary dramatically within the respective conditions of each stage. Furthermore, while previous work suggested that wake physics within polar craters diverts solar wind protons toward the crater floor (where they may represent a significant source of implanted hydrogen) [Zimmerman et al. 2011, Farrell et al. 2010], one stage of the CME introduces a significant population of heavier, highly-charged He^{++} ions that may also perturb the balance of volatiles at the surface.

For convenience a CME event observed by *Skoug et al. 1999* is divided into four distinct temporal stages: typical solar wind; a dense, hot shock; a faster-flowing, cooler early cloud; and, a dense, cold late cloud (e.g., Table 1) [Farrell et al., submitted to this issue, 2012]. The constituent environmental conditions are simulated using the open-source kinetic plasma code XOOPIC [Verboncoeur et al. 1995] incorporating an idealized, dielectric lunar surface and open boundary conditions on the solar wind plasma. Details of the kinetic code and simulation set, as well as conclusions regarding variations in wake structure during passage of the storm are presented in Section 2. Particle currents are extracted at representative locations at the surface and fed forward into the astronaut charging model of Jackson et al. 2011, modified to include an accounting of secondary electron emission from the astronaut suit. Section 3 contains a description of this charging model and presents results on the charging characteristics of insulating and conducting astronaut suits during the storm. Finally, Section 4 contains a discussion

of the implications for volatile sputtering and sequestration due to the various proton and heavy ion fluxes encountered during the storm.

2. Kinetic simulations of wake density, electric field, potential, and particle fluxes

2.1. Kinetic simulation setup

The simulation approach is largely as described in Zimmerman et al., 2011. The open-source 2D kinetic plasma code XOOPIC [Verboncoeur 1995] is used to simulate an idealized, step-like, dielectric crater topography. This simplification of shape, which is illustrated in Fig. 1, reveals the governing physics in a clear and straightforward manner. Maxwellian populations of electrons and protons are injected at the upstream and overhead boundaries to provide a continuous flow of plasma particles into the system. Slight modifications were made to the code to enable a self-consistent flow of particles through the downstream boundary. Electrons with horizontal velocity greater than $2v_{sw}$, where v_{sw} is the solar wind drift speed (measured in m s^{-1}) are recycled at the downstream boundary to simulate the backward-moving portion of the electron population as it responds to upstream conditions. All other particles exiting through open boundaries of the simulation domain are discarded. Otherwise, the particle trajectories evolve according to the locally self-consistent electric field including contributions from charges that have impacted and been recorded at the surface.

The ion population is represented using a downward-moving, half-Maxwellian velocity distribution to capture the fact that upward-moving ions will have been absorbed by the dayside lunar surface far upstream. The magnetic field is

assumed to be zero everywhere, as a typical electron undergoes about 3% of a gyration (about an interplanetary magnetic field line) while traversing the entire depth of the crater; the validity of this assumption has been verified through a handful of simulations with a nonzero interplanetary magnetic field. It is known that surface-reflected protons from the lunar dayside can reach polar and nightside regions after gyration within the interplanetary magnetic field [Nishino et al., 2009]; however, non-ambipolar ion entry into polar craters is beyond the scope of the present paper, and we do not attempt to model global-scale ion pickup in the present, regional-scale simulations.

The electric field components at the crater surface are affected by the locally accumulated surface charge according to the boundary conditions imposed by Maxwell's equations [Verboncoeur et al. 1995], and the surface charge is naturally zero at the open solar wind boundaries. An electric potential gauge of zero volts is imposed at the overhead boundary. Secondary electrons are emitted by primary electron impacts using the yield-vs.-impact energy curve of Vaughan 1989, parameterized to model the experimentally-measured yield of lunar regolith [Willis 1973]. Secondary emission by ion impacts (i.e. sputtering) is not included in the present model. Small variations in the net ion current due to sputtering of other ions (or neutral sputtering products, which would carry zero electric current) are of much less importance to overall electrostatic properties of the wake than the interplay between primary and secondary electron emission [Zimmerman et al. 2011].

The crater depth h_{cr} was chosen to be at least tens of Debye lengths λ_{sw} deep under the dynamic range of conditions imposed by the passing storm (h_{cr} and λ_{sw} are measured in units of m). The condition $\lambda_{sw}<<h_{cr}$ is representative of large craters at the lunar poles (λ_{sw}~15 m for the typical solar wind); thus, a range of crater depths from 250-1000 m deep was simulated. The primary simulation data plotted in Figs. 2-5 and 7 were taken from the 250 m-deep crater subset; however, the effects of crater depth are discussed in Section 2.2 and shown in Fig. 6. The simulation grid spacing is chosen to be less than λ_{sw} during each CME stage. It is computationally unfeasible to vary the plasma conditions continuously over a simulated timescale of days, so each stage of the passing CME is simulated independently according to the solar wind parameters given in Table 1. In most cases, only a small amount of simulated time corresponding to tens of ion plasma periods is required to reach a quasi-steady state, after which the resultant fields and computed fluid quantities such as particle density and flow speed were time averaged for hundreds of ion plasma periods.

2.2. Basic modulation of wake structure by passage of the storm

Figure 2 shows basic results from the kinetic plasma simulations described in Section 2.1, including net charge concentration, electric field, and electric potential structure within a 250 m-deep crater during each stage of the passing storm. Under typical solar wind conditions (Fig 2a) electrons race into the crater ahead of the slower ions, forming a persistent non-neutral cloud of negative space charge. An ambipolar electric field sets up between the negative electron cloud and positive ions at the wake flank, and the thermal ion population enters the crater via

acceleration by the ambipolar field. The entire ambipolar field region is roughly a few λ_{sw} deep. A negative surface potential forms all along the surface; however, the potential is most negative in the region where electrons reach the crater floor accompanied by relatively few protons. Farther downstream the plasma environment returns toward a "wall sheath" configuration in which the near-surface space charge density is positive, the surface potential is negative, and the horizontal variation in structure diminishes. It will be shown that the basic structural components of the wake including the ambipolar charge separation, ambipolar electric field and potential, and surface potential, as well as the flux of plasma particles to the surface, are modulated by changes in solar wind conditions as the storm passes by.

It is worth noting that the system reaches a quasi-steady state when current balance (i.e. net zero electric current) is achieved everywhere along the surface. In the kinetic simulations employed, the particle currents at the surface are statistical in nature: at any given time and location an integer (or zero) number of incident particles perturbs the local charge distribution, emitting secondary electrons and generating a local plasma response. Thus, averaging over many snapshots of the particle flux to the surface produces a quasi-steady, statistical depiction of the surface fluxes, shown in Figure 3. Underneath the electron cloud the primary and secondary electron fluxes generally balance one another, being roughly an order of magnitude more intense than the local ion fluxes (except in the late cloud case where secondary emission is relatively low). Ions are also important in establishing

current balance farther downstream because the plasma expansion delivers a significant population of ions as well as primary electrons to the surface.

In the "shock" stage of the storm the bulk plasma density n_0 is four times higher and the electron temperature T_e is almost an order of magnitude higher than in the typical solar wind. The parameters n_0 and T_e have units of m^{-3} and K, respectively. It is easily seen from Fig. 2b that the resulting increase in electron flux into the crater strengthens the ambipolar field and significantly enhances the negative surface potential everywhere. Secondary emission, which is roughly linear in T_e in the regimes considered herein, increases during the shock and enhances the charge density within the negative electron cloud region. In contrast with the other stages of the storm, there is a significant population of secondary electrons near the surface much farther downstream, as denoted in Fig 2b. In fact, the surface is charged positive because the average secondary yield is above unity for the enhanced primary electron energies of the present case. Interestingly, formation of the ambipolar potential causes the surface to float negatively with respect to the bulk plasma, although the surface continuously emits secondary electrons and remains positive. The emitted secondary population forms a cloud of negative charge near the surface but since the potential rises monotonically with increasing height all emitted secondary electrons escape the surface. The current due to secondary emission from the surface must be included when modeling charging of human exploration infrastructure (cf., Section 3).

The "early cloud" stage follows the shock stage with plasma parameters similar to the typical solar wind. The resulting plasma wake is depicted in Fig. 2c,

showing a clear resemblance to the typical solar wind stage with respect to the magnitude of the ambipolar charge separation and electric field and potential structure. Perhaps the most notable difference between the early cloud and typical solar wind cases is that the wake appears to be "stretched" horizontally during passage of the early cloud; this is due to an increase in solar wind speed v_{sw} relative to the characteristic ion vertical speed as represented by c_s (measured in m s^{-1}). The issue of variations in spatial scale will be considered more comprehensively in Section 2.3. Finally, during the "late cloud" stage, n_0 is relatively high (about a factor of 15 greater than the typical solar wind) and T_e is relatively low (about a factor of four lower than the typical solar wind). The most notable effect is that λ_{sw} is significantly reduced, thereby compressing the vertical scale of the ambipolar region by nearly an order of magnitude.

In all cases, the density profile just above the crater wall sets the initial conditions for plasma expansion into the crater. However, in the late cloud it is obvious that fine details of the plasma sheath on the upstream plateau (outside and upstream of the domains of Fig. 2) can propagate far downstream (e.g. the blue streamer of positive space charge in Fig. 2d). The same feature is evident to varying degrees in some of the other simulations, but these "positive streamers" have a negligible effect on the large-scale structure of their parent wakes.

2.3. Dimensional analysis and detailed variation of wake structure

There are numerous physical parameters that govern the structure of a plasma wake near a dielectric, charge-collecting surface. These parameters include those already defined, as well as the peak secondary electron emission coefficient δ_0

(dimensionless) and electron impact energy at peak emission E_0 (eV), and are listed in Table 1. From this collection of physical variables four dimensionless ratios have been constructed:

$$\alpha = \frac{v_{sw}}{c_s} \quad \text{(wake inflow angle, or ion Mach number)} \quad (1)$$

$$\eta = \frac{h_{cr}}{\lambda_{sw}} \quad \text{(effective obstruction size)} \quad (2)$$

$$\zeta = \frac{k_B T_e / e}{E_0} \quad \text{(normalized electron impact energy)} \quad (3)$$

$$\delta_0 \quad \text{(secondary electron yield)} \quad (4)$$

where k_B is Boltzmann's constant (J kg^{-1} K^{-1}) and e is the electron charge (C) which have been introduced to express the electron temperature in units of eV, commensurate with the units of E_0. The ratio α represents the characteristic inflow angle of the ions with respect to the solar wind drift velocity vector, and will be shown to govern the horizontal and vertical spatial scales of the wake (α is equivalently the ion Mach number). The ratio η captures the effective depth of the crater with respect to the thickness of the ambipolar charge separation region. The ratio ζ characterizes the amount of secondary emission from the surface at a given solar wind temperature and constant secondary electron yield. It will be shown that together η and ζ govern the electric field and potential structure of the wake by controlling the interplay between surface and ambipolar electric fields. The effects of δ_0 have been previously explored by *Zimmerman et al., 2011* and are not further investigated herein. Values for the parameters (1)-(4) during the solar storm are given in Table 1.

2.3.1 Variations in horizontal and vertical spatial scales of plasma wakes

The overall spatial scale of the wake is governed by properties of the ions since they carry a large fraction of the total inertia in the system. As mentioned previously, the primary velocity scales governing ion inflow are the solar wind convection speed v_{sw} and the ion sound speed c_s. The canonical theory of quasineutral plasma expansion [Farrell et al. 2010, Mora and Pellat 1979, and references therein] suggests that these velocity scales may be wrapped into a "self-similar" dimensionless ratio parameterizing the ion density in the expansion region,

$$\xi = \left(\frac{h_{cr} - y}{x}\right)\frac{v_{sw}}{c_s} \tag{5}$$

where x and y are the horizontal and vertical distance from the bottom corner of the crater wall (e.g. the top rim of the crater is located at x=0, y=h_{cr}). Note that v_{sw}/c_s is simply the ion Mach number given by (1). For cold ions the number density may be written purely as a function of ξ [Mora and Pellat, 1979],

$$n_i = n_0 \exp(\xi + 1) \tag{6}$$

Expressions (5) and (6) are particularly useful because they capture the spatial scaling of the wake in terms of background solar wind flow conditions as well as the obstruction size. For instance, multiplying the velocities of (5) by the basic ion plasma timescale $\omega_{pi}^{-1}=(v_{the}/\lambda_{De})^{1/2}$ (units of s) yields the horizontal and vertical length scales of the system, which are respectively $v_{sw}\omega_{pi}^{-1}$ and $c_s\omega_{pi}^{-1}$, and are listed in Table 1 for the stages of the passing CME. In the present work $c_s\omega_{pi}^{-1}$ is equivalent to the plasma Debye length; however, this will not be the case in more general scenarios where the ions and electrons are not in thermal equilibrium. Varying

either of the length scales $v_{sw}\omega_{pi}^{-1}$ or $c_s\omega_{pi}^{-1}$ (or, equivalently, the velocity scales v_{sw} or c_s) modifies the ratio (1) and stretches or compresses the geometry of the wake.

In Figure 4 (top row) the normalization length scales $v_{sw}\omega_{pi}^{-1}$ and $c_s\omega_{pi}^{-1}$ are validated against the expanding ion density contours across the wide range of conditions encountered during passage of the CME. The non-dimensionalized density contours remain roughly unchanged during the entire storm, indicating that the chosen normalization length scales capture the overall spatial structure of the wake. Furthermore, the equal-density contours from theory (Eq. 6) are straight lines fanning out from the crater rim, and the simulated contours of ion density in Fig. 4 are indeed quite linear, at least downstream of $x=v_{sw}\omega_{pi}^{-1}$. Upstream of this region the canonical theory cannot be applied because it does not account for the strong separation of charge near the crater wall; in this upstream region the ion density contours curve gently in the simulations. Finally, Fig. 4 (as well as the density contours of Fig. 2, top row) shows that within the expansion region the ion density falls off exponentially with decreasing height, which is consistent with expression (6).

The mismatch between the density contours of the middle and top rows of Fig. 4 (and the top row of Fig. 2) fortifies the conclusion that electrons do not strictly follow the ion flow; the lighter, faster electrons not only outpace the ions entering the crater, but also produce and quickly respond to local electric fields. The low-energy bulk of the electron distribution penetrates a few λ_{sw} into the wake and is reflected back into the solar wind by the ambipolar field, indicated by a "bulge" in the electron population below the wake flank. The fastest electrons escape the

ambipolar region and continue toward the surface where they accumulate to form a surface electric field and associated negative potential. Fig. 4 (bottom row) demonstrates a topological similarity between the potential structure and the electron density, stemming from the fact that plasma electrons within the non-neutral region constitute the source term in Poisson's equation for electric potential. In short, while electrons play a critical role in driving the ambipolar expansion it is the properties of the ions – namely $v_{sw}\omega_{pi}^{-1}$ and $c_s\omega_{pi}^{-1}$ – that determine the overall scale of the wake. Essentially, solar wind electron pressure generates the wake's electric field against the structural backdrop provided by ion inertia.

2.3.2 Variations in the electric potential and electric field of plasma wakes

Figure 5a compares representative vertical profiles of the vertical electric field across the wide variety of conditions encountered during the CME. The profiles are taken at a horizontal location x=0.5$v_{sw}\omega_{pi}^{-1}$ to exploit the horizontal scaling of the wake, providing consistency across all cases (see Table 1 for values of $v_{sw}\omega_{pi}^{-1}$). The peak ambipolar field E_{amb} is on the order of the characteristic electric field $k_BT_e/e\lambda_{sw}$, which is consistent with theory [Crow et al. 1975; Mora and Pellat 1979]. At very low levels of secondary emission (as parameterized by ζ) the surface can accumulate a large net amount of negative charge from the primary electron cloud, and the resulting surface electric field E_{srf} grows to envelope the entire non-neutral region [cf. Zimmerman et al., 2011]. This effect is clearly evident in the case of the late-cloud, in which the nearly uniform E_{srf} extends from the surface into the ambipolar region. In other words, there are two components to the wake's electric

field: the ambipolar field and the surface field due to accumulated surface charge, and the parameter ζ governs the balance between the two field components.

In all of the cases herein, the ambipolar field is the strongest component, evidenced by Fig. 5a. Also, Fig. 5b shows the corresponding potential structure of each case, where it is clear that a total potential drop from plasma to surface on the order of tens of $k_B T_e/e$ is possible. Within a few λ_{sw} below the wake flank the space potential Φ tends to reach a few $k_B T_e/e$ due to the ambipolar expansion process. During the late cloud stage the magnitude of Φ clearly continues to increase with depth into the crater. There is a combination of effects giving rise to the very large potential drop during the late cloud. First, T_e falls considerably with respect to the other stages, causing secondary emission to drop via a reduction in ζ and allowing E_{srf} to extend throughout the expansion region (e.g. the "flat" electric field profile deep within the crater). Second, the Debye length shrinks considerably, causing an increase in η. As a result, E_{srf} integrates over a larger depth with respect to the very shallow ambipolar region to form a large potential drop.

For a larger collection of runs including craters of different depths, the effects of secondary emission and crater depth are captured by the two dimensionless ratios ζ and η. Fig. 6a shows that the normalized potential drop $\varphi = e\Phi_{tot}/k_B T_e$, or potential "amplification", responds to the amount of secondary emission as parameterized by ζ [cf. Zimmerman et al. 2011]. In addition, Fig. 6b shows that φ generally becomes more negative with increasing crater depth. The simulations span two important regimes of η where the ambipolar region is either partially or fully formed. In the former case where the crater is effectively shallow (e.g., $\eta<20$)

the vertical space required to form the full ambipolar charge separation (about $10\lambda_{sw}$ according to *Crow et al. 1979*) is hardly available. In this regime solar wind electrons must overcome E_{amb} integrated over a few λ_{sw}; thus, the normalized potential φ is relatively small. In the opposite high-η extreme (e.g. the late cloud), the crater is effectively much deeper than λ_{sw}, and even a weak E_{srf} can then integrate over many λ_{sw} to create a large φ. In the η>100-200 regime the charging timescale within the electron cloud appears to be much longer than the simulated time, and the numerical limit on the electric potential ($\sim 30T_e$) is approached asymptotically (cf. Zimmerman et al. 2011). Thus, the late cloud potentials shown in Fig. 6b are in a state of slowly approaching the simulation limit but it would take an unfeasible computation time for the potentials to saturate. However, when compared to the other stages of the CME, all of the late cloud potentials of Fig. 6b demonstrate that there is a clear increase in $|\varphi|$ with increasing crater depth as parameterized by η.

3. Astronaut charging in the regional wake environment

3.1. Object Charging Model

The constituent particle fluxes from each stage, shown in Figure 3 and listed in detail in Table 2, were fed forward into an equivalent circuit model of astronaut charging to anticipate the electrical hazards of stepping across the crater surface. The charging model was originally developed in Jackson et al. 2011, and is modified herein to include secondary emission from the astronaut suit. During each stage of the passing CME, the model provides an accounting of the triboelectric and plasma charges accumulated by an astronaut moving in periodic steps (every 10 seconds)

about a given location on the crater floor. To find the object potential relative to the solar wind plasma potential, a charging equation is solved given the local particle fluxes and secondary emission coefficient, δ_{eff}~0.5-0.99, for the astronaut suit. The primary assumptions in the charging model are that the astronaut suit is smaller in scale than the local Debye length and is immersed in electron and ion currents consistent with the equilibrium surface charge state. The latter criterion is automatically satisfied by the particle fluxes everywhere along the surface in the PIC simulations, and a spacesuit of about 1.5 m in height is considered, which has been verified to be much smaller than the local Debye length throughout the plasma expansion region (cf. Table 1).

3.2. Astronaut charging rates and existence of charge equilibrium

Two spatial locations representing regional environmental extremes are chosen including an upstream location (x_1=250 m) within the tenuous, non-neutral expansion region and a downstream location (x_2=1500 m) where the plasma density and ion fluxes are significantly greater. The charging and discharging behavior of an astronaut stepping in the vicinity of x_1 and x_2 is shown in Figure 7. In this set of runs, the astronaut suit is considered to be insulating, with a low effective "triboelectric capacitance"; that is, the boot sole voltage acquired via accumulation of triboelectric charge is -13.6 V/step, as in Jackson et al. 2011. The secondary emission coefficient of the insulating suit is δ_{eff}=0.5 [Jackson et al. 2011, Farrell et al. 2010].

Under typical solar wind conditions within the expansion region (i.e., at x_1) the suit potential becomes more negative with each step due to triboelectric charge accumulation (e.g. Fig. 7a). In the absence of strong plasma currents, triboelectric

charge accumulation effectively becomes perpetual; that is, charge is not dissipated at a rate faster than the astronaut's 10 s-per-step cadence. Much farther downstream (i.e., at x_2 in the presence of enhanced particle fluxes including a significant contribution from solar wind ions) charge is more quickly dissipated and the astronaut will return to the same equilibrium potential of about -10 V, or roughly $-T_e$, in the 10 s before taking the next step (e.g. Fig. 7b).

Model results considering an astronaut exposed to the shock passage are shown in Figure 7c,d. Throughout the entire crater the astronaut's accumulated charge will quickly dissipate between individual steps due to the enhanced flux of all plasma species during this warm, dense stage. Overall, the astronaut's potential during the shock stage is more negative than in exposure to the typical solar wind because of the increased number of secondary electrons near the surface and the enhanced primary electron flux both due to increased n_0 and T_e. More specifically, the astronaut's equilibrium potential is about -50 V if roving upstream at x_1 and -15 V downstream at x_2; the difference is due primarily to an upstream surplus of primary and secondary plasma electrons relative to the local density of ions. Interestingly, Figure 3 shows that in the upstream electron cloud region the total electron flux surpasses the ion flux by roughly a factor of about 100 but farther downstream the ratio is only about 10; thus, when located upstream (underneath the negative electron cloud) the astronaut floats to a more negative potential.

Figure 7e,f shows results for astronaut exposure to environmental conditions during the early cloud. The charging and dissipation characteristics are similar to those encountered in the presence of typical solar wind conditions, which is a

consequence of the similarity in T_e and n_0 between the two stages. As in the typical solar wind case, the astronaut floats more negatively with each step when roving upstream and tribocharging becomes perpetual in the absence of adequate charge remediation by environmental currents. Farther downstream the astronaut reaches an equilibrium potential of about -10 V.

Finally, Figure 7g,h shows that during the very tenuous, cold late cloud the astronaut can be expected to charge indefinitely while walking upstream in the vicinity of x_1, similar to the typical solar wind and early cloud cases. When roving about location x_2 downstream, the astronaut is able to remediate charge and come to an equilibrium potential of about -10 V before taking the next step.

The next set of runs considers the same insulating astronaut suit now exposed to a relatively high triboelectric capacitance scenario in which the boot sole potential changes by 136 V per step. The results are qualitatively similar to those of Figure 7. In general, at 10 steps per second the astronaut's triboelectric charge accumulation dominates over the environmental plasma currents, and the suit potential diverges, as in Fig. 7a. The average divergence rate is generally slowest in exposure to the downstream plasma, due to the increased plasma fluxes providing more significant charge remediation there. However, there is still an overall perpetual charging behavior irrespective of the plasma conditions. It is notable that in the present scenario of Fig. 7 the electric potential reaches significantly higher levels of -300 V to -3000 V during the same one-minute period simulated in Fig. 7. The only set of conditions under which the suit actually reaches charge equilibrium is within the downstream environment of the warm, dense shock where the particle

fluxes are significantly enhanced; here, the equilibrium potential is about -50 V, as in the case of Fig. 7d where the solar wind current source dominates over the tribocharging process. In a real lunar wake astronaut charging would eventually be limited by some other factor such as electrical discharging via physical contact with or proximity to local infrastructure, the finite excursion time associated with a moonwalk, field emission from sharp edges on the suit, or nonlinear feedback limiting the local plasma fluxes.

For comparison, the charging dynamics of a fully conducting suit were also considered, with a secondary emission coefficient δ_{eff}=0.99 characteristic of a conductor at the primary electron energies modeled herein [Jackson et al., 2011, Farrell et al., 2010]. The behavior closely resembles that of the insulating case therefore figures are not included. The principal difference between the conducting and insulating suits is in their composition relative to the surface [Jackson et al. 2011], allowing greater triboelectric charge accumulation by the conducting suit counterbalanced by a simultaneous decrease in suit capacitance (cf. Jackson et al. 2011 for more details).

4. Implications for the volatile balance within a PSR

The fact that solar wind protons are accelerated into the crater by the wake electric field has implications for the sequestration and loss of volatiles at the crater floor. It has previously been argued on the basis of laboratory experiments [e.g., Johnson, 1989] that for a crater floor nearly devoid of water ice the H_2O sputtering yield induced by solar wind proton bombardment (at the 1 keV energies observed in the simulations) will be approximately 0.01 molecule per incident proton

[Zimmerman et al. 2011, Farrell et al. 2010, Crider and Vondrak 2003, and references therein]; in this case, solar wind protons will represent a source of hydrogen to the surface. However, for a water-rich surface the sputtering yield for water increases to near unity [Johnson, 1989], so in this scenario proton bombardment would serve to scour water from the surface (e.g. Table 3).

Other solar wind ions may play a role in sputtering a wide variety of volatiles during passage of the solar storm. Of particular interest in the present work is the increase in He^{++} (doubly-ionized He) density to about 20% of the proton density during passage of the early cloud [Skoug et al. 1999]. Although He^{++} ions were not explicitly included within the simulations, the self-similar formalism presented in Section 2.3 may be exploited to estimate the amount of sputtering induced by He^{++}. The sputtering yield goes roughly as $(MZ^2)^s$ where the exponent s falls within the range 1-1.6 [Johnson, 1990; Elphic, 1991]; thus, the characteristic sputtering rate due to He^{++} impacts is anticipated to be as high as $(4 \cdot 2^2)^{1.6} \sim 85$ times the rate due to proton impacts under typical solar wind conditions. By analogy with solar wind protons, the He++ impact rate will vary with position along the surface due to the ambipolar expansion process (e.g., Fig. 1). Assuming thermal equilibrium between plasma species, the He^{++} sound speed (characterizing the He^{++} inflow rate) will be half the proton sound speed; thus, the bulk population of He^{++} ions will reach the surface at roughly twice the distance downstream. The characteristic He^{++} flux during the early cloud is estimated to be about 0.1 times the characteristic proton flux – that is, $(n_{He++}/n_0)(c_{sHe++}/c_s)=(0.2)(0.5)=0.1$ – giving an effective maximum sputtering yield as high as $85 \cdot (0.8\ H_2O/\text{proton})(0.1 \cdot n_0 c_s) \sim 7.3 \times 10^{11}\ H_2O\ m^{-2}\ s^{-1}$ for

an icy regolith or $85 \cdot (0.01\ H_2O/\text{proton})(0.1 \cdot n_0 c_s) \sim 9.2 \times 10^9\ H_2O\ m^{-2}\ s^{-1}$ for a pure silica surface.

More generally, integrated sputtering over many extreme solar wind events could play a role in determining the abundance of hydrogen on equator-facing shadowed slopes (i.e., slopes with normal vector pointing toward the equatorial plane of the Moon); however, the average implantation and sputtering rates during a typical lunation are currently poorly constrained for real topography. Nevertheless, the present simulation results suggest that within narrow, deep topographic features any accumulated water and other volatile species will generally be shielded from sputtering by protons and heavier ions. A sub-crater within a larger PSR may provide the most favorable environment for volatile sequestration by combining the effects of topographic shielding with shielding from photons scattered at the rim of the parent crater, or "double thermal shielding" [Colaprete, 2012]. In this scenario the sub-crater floor is able to maintain an extremely low temperature at which accumulated water is maximally stable while also being protected from scouring by the highly-variable solar wind. Such a hypothesis could explain the relatively high abundance of water detected within the LCROSS impact plume [Colaprete et al., 2010] with respect to the water concentrations inferred from LEND epithermal neutron measurements [Mitrofanov et al., 2010]. Furthermore, a highly topography-sensitive process – such as regional plasma wake formation – influencing the sequestration of volatiles at the lunar poles could also help to explain the enigmatic lack of spatial correlation between the locations of highest inferred water concentrations and regions of permanent

shadow [Mitrofanov et al., 2010], although a more detailed understanding of wake formation in the vicinity of complex lunar topography is needed.

5. Conclusions

It is found that the physical parameters affecting wake structure in the vicinity of a step-like lunar crater may be distilled into at least four leading dimensionless ratios including $\alpha=v_{sw}/c_s$, $\eta=H/\lambda_{sw}$, $\zeta=T_e/E_0$, and δ_0, which represent the characteristic solar wind inflow angle, effective depth of the crater with respect to the ambipolar region, and secondary emission properties, respectively (Eq. 1-4). During a solar storm a stationary observer at the surface would observe changes in the particle fluxes and ambipolar field as the local self-similar parameter ξ varies with changing v_{sw}, c_s, and λ_{sw} (Eq. 5-6). Solar wind electrons form and quickly respond to local electric fields within the structural backdrop provided by the expanding ion population, and secondary emission plays a prominent role in establishing equilibrium current balance in regions where electrons predominantly reach the surface. In particular, changing the constituent velocities v_{sw},and c_s within the ratio α affects the horizontal and vertical spatial scaling of the wake. Decreasing the ratio ζ decreases the overall amount of secondary emission, and allows a very large negative potential to develop underneath the electron cloud, up to a magnitude of tens or hundreds of T_e. Increasing the ratio η also tends to increase the wake potential drop.

Environmental particle fluxes were fed forward from the kinetic simulations into a model of triboelectric astronaut charging. The astronaut is considered to be electrically isolated so that plasma and secondary emission currents provide the

only paths to remediation of accumulated triboelectric charge. A stepping rate of one step per 10 s was assumed, with the astronaut gaining negative triboelectric charge at each step. An equilibrium suit potential exists only in cases with enhanced particle fluxes (through increased n_0 or T_e); if the plasma currents are relatively low then suit will collect triboelectric charge until some other process mitigates the significant electron buildup on the suit (e.g., field emission, secondary emission via cosmic rays, etc. [Zimmerman et al., 2011]). Thus, for an insulating suit the hot, dense shock stage of the CME is the most favorable for avoiding perpetual charging of the astronaut suit; however, this period is the most hazardous with respect to other factors such as high-energy particle fluxes and radiation.

The wake formation process may play a leading role in volatile sequestration and sputtering within PSRs. Heavier, highly-charged ions such as He^{++} observed within the early cloud stage of the CME by *Skoug, 1999* would tend to scour water away from the surface. However, it is suggested that narrow, deep polar features or sub-craters within larger PSRs are prime environments for protecting accumulated volatiles via (1) topographic shielding from heavier ions and (2) double thermal shadowing in which scattered sunlight cannot reach the sub-crater surface to sublimate volatile species. Topographic modulation of solar wind particle fluxes may help to provide an explanation for the enigmatic spatial distribution of surficial water at the lunar poles; however, a more detailed understanding of wake formation downstream of real lunar topography, over many lunations and extreme solar wind events, is required to fully address this issue. Simulation efforts are underway to

generalize the results presented herein to a broader range of topographic geometries and scales.

Acknowledgements

We gratefully acknowledge the generous allocation of NASA Goddard Space Flight Center computing resources by Tim McClanahan. This research was supported by an appointment to the NASA Postdoctoral Program at the Goddard Space Flight Center, administered by Oak Ridge Associated Universities through a contract with NASA. The support of LPROPS grant NNX08AN76G and the NASA Lunar Science Institute and DREAM virtual institute through grant NNX09AG78A are gratefully acknowledged.

References

Colaprete, A., et al. "Detection of water in the LCROSS ejecta plume", Science 330, 463 (2010).

Colaprete, A. "Lunar PSRs: A review of recent measurements and discoveries", Lunar Superconductor Applications 2 Conference, The Woodlands, TX, March 16, 2012.

Crider, D. H., and R. R. Vondrak. "Space weathering effects on lunar cold trap deposits", J. Geophys. Res., 108, 5079 (2003).

Crow, J. E., P. L. Auer and J. E. Allen. "The expansion of a plasma into a vacuum", J. Plasma Phys., 14, 65 (1975).

Elphic, R. C., H. O. Funsten III, B. L. Barraclough, D. J. McComas, M. T. Paffett, D. T. Vaniman, Heiken, G. "Lunar surface composition and solar wind-induced secondary ion mass spectrometry", Geophys. Res. Lett 18, 2165 (1991).

Farrell, W. M., T. J. Stubbs, J. S. Halekas, R. M. Killen, G. T. Delory, M. R. Collier, and R. R. Vondrak. "Anticipated electrical environment within permanently shadowed lunar craters", J. Geophys. Res. 115, E03004 (2010).

Farrell, W. M. et al., submitted to J. Geophys Res. (2012).

Jackson, T. L., W. M. Farrell, R. M. Killen, G. T. Delory, J. S. Halekas, and T. J. Stubbs. "The discharging of roving objects in the lunar polar regions", J. Spacecraft and Rockets 48, 700 (2011).

Johnson, R. E. Energetic Charged Particle Interactions With Atmospheres and Surfaces; Chapter 3, Spinger, New York (1989).

Killen, R. M., et al. "The effect on the lunar exosphere of a coronal mass ejection passage.", J. Geophys. Res. 117, E00K02 (2012)

Mitrofanov, I. G. et al. "Hydrogen mapping of the Lunar south pole using the LRO neutron detector experiment LEND", Science 330, 483 (2010).

Mora, P. and R. Pellat. "Self-similar expansion of a plasma into a vacuum", Physics of Fluids 22, 2300 (1979).

Neal, C. R., "The Moon 35 years after Apollo: What's left to learn?", Chemie der Erde – Geochemistry, 69, 3 (2009)

Nishino, M. N., et al., "Solar wind proton access deep into the near-Moon wake", Geophys. Res. Lett, 36, L16103 (2009)

Paige, D. A., et al. "Diviner Lunar Radiometer Observations of Cold Traps in the Moon's South Polar Region", Science 330, 479 (2010).

Poppe, A. and M. Horanyi. "Simulations of the photoelectron sheath and dust levitation on the lunar surface", J. Geophys. Res. 115, A08106 (2010)

Shearer, C. K. and C. Neal. "Strategic Knowledge Gaps for the 'Moon First' Human Exploration Scenario", Lunar Exploration Working Group, http://www.lpi.usra.edu/leag/GAP_SAT_03_09_12.pdf (2012)

Skoug, R. M., et al. "A prolonged He+ enhancement within a coronal mass ejection in the solar wind", Geophys. Res. Lett., 26, 161 (1999).

Vaughan, J. R. M. "A New Formula for Secondary Emission Yield", IEEE Trans. Electron Dev., 36, 1963 (1989).

Verboncoeur, J. P., A. B. Langdon and N. T. Gladd, "An Object-Oriented Electromagnetic PIC Code", Comp. Phys. Comm., 87, May 11, 1995, pp. 199-211.

Willis, R. F., M. Anderegg, B. Feuerbacher, and B. Fitton. "Photoemission and secondary electron emission from lunar surface material", Photon and Particle Interactions with Space, Proc. 6th ESLAB Symp. 37, 389 (1973).

Zimmerman, M. I., W. M. Farrell, T. J. Stubbs, J. S. Halekas, and T. L. Jackson. "Solar wind access to lunar polar craters: Feedback between surface charging and plasma expansion", Geophys. Res. Lett. 38, L19202 (2011).

Figure Captions

Figure 1: Illustration of plasma expansion process including behavior of electrons, protons, and He^{++} ions.

Figure 2: Simulated plasma conditions within a polar lunar crater during passage of the modeled CME. Plasma parameters during each stage of the storm are given in

Table 1. Blue and red density contours correspond to $\log_{10}$ proton and net electron density, respectively, each normalized to the bulk solar wind density (n_0) before applying the logarithm. *Net charge concentration levels in column (d) have been amplified by a factor of 10 to reveal the relatively weak charge separation along the wake flank.

Figure 3: Simulated particle fluxes at the surface of the crater of Figure 2. Dots represent the time-averaged flux at each surface point, while solid lines depict a running spatial average along the surface. Electrons and ions are moving toward the surface (positive absolute particle flux to the surface), while emitted secondary electrons are moving away from the surface (negative absolute particle flux).

Figure 4: Contours of $\log_{10}$ ion density (top), $\log_{10}$ electron density (middle), and electric potential (bottom) from the cases in Figure 2, with spatial units scaled by $\omega_{pi}^{-1}v_{sw}$ and $\omega_{pi}^{-1}c_s$ along the horizontal and vertical axes, respectively. Particle densities are normalized by n_0 before applying the logarithm, and electric potential is normalized to k_BT_e/e and plotted on a linear scale.

Figure 5: Vertical profiles of the normalized, vertical electric field and normalized electric potential taken at x=0.5$\omega_{pi}^{-1}v_{sw}$ within the 250 m-deep crater of Figure 2.

Figure 6: (a) Normalized total electric potential drop at at x=0.5$\omega_{pi}^{-1}v_{sw}$ versus amount of secondary electron emission for a collection of 250 m-, 500 m-, and 1000

m-deep craters. An increase in ζ^{-1} implies an effective decrease in secondary emission. (b) Normalized total electric potential drop at $x=0.5\omega_{pi}^{-1}v_{sw}$ versus normalized crater depth.

Figure 7: Charging history of an insulating astronaut suit at x_1=250 m (a,c,e,g) and x_2=1500 m (b,d,f,h) within the 250 m-deep crater of Fig. 2, at an astronaut stepping rate of 1 step per 10 s.

Tables

	Typical	Shock	Early Cloud	Late Cloud
n_0 (10^6 m^{-3})	5.0	20	3.0	70
v_{sw} (km s^{-1})	450	600	650	500
T_e (10^4 K)	9.98	80.0	8.00	3.02
v_{the} (km s^{-1})	1740	4930	1560	954
c_s (km s^{-1})	40.6	115	36.4	22.3
ω_{pe} (kHz)	126	252	97.7	472
ω_{pi} (kHz)	2.94	5.89	2.28	11.0
λ_{sw} (m)	13.8	19.5	15.9	2.03
E_0 (eV)	300	300	300	300
δ_0	1.5	1.5	1.5	1.5
$v_{sw}\omega_{pi}^{-1}$ (m)	153	102	285	45.5
$c_s\omega_{pi}^{-1}$ (m)	13.8	19.5	15.9	2.03
$\alpha=v_{sw}/c_s$	11.0	5.2	17.9	22.4
$\eta=H/\lambda_{sw}$	36.2	25.6	31.4	250
$\zeta=k_BT_e/eE_0$	0.029	0.23	0.023	0.009
δ_0	1.5	1.5	1.5	1.5

Table 1: Bulk plasma parameters, secondary emission parameters, horizontal and vertical scaling lengths, and leading dimensionless ratios during passage of the modeled solar storm.

Current Density ($A\,m^{-2}$)	Typ. Solar Wind		Shock Passage		Early Cloud		Late Cloud	
	250m	1500m	250m	1500m	250m	1500m	250m	1500m
Ions	1.6×10^{-11}	7.5×10^{-9}	1.6×10^{-9}	1.6×10^{-7}	1.6×10^{-11}	2.1×10^{-9}	6.4×10^{-11}	4.8×10^{-9}
Electrons	5.1×10^{-10}	1.6×10^{-8}	1×10^{-7}	4×10^{-7}	2.1×10^{-10}	4×10^{-9}	2.1×10^{-10}	7.2×10^{-9}
Secondaries	5.1×10^{-10}	4×10^{-9}	8×10^{-8}	3.2×10^{-7}	1.6×10^{-10}	1.3×10^{-9}	3.2×10^{-11}	1.6×10^{-9}

Table 2: Ion, electron, and secondary electron currents deep within the upstream wake expansion region (at x_1=250m) and much farther downstream (at x_2=1500m), taken from the kinetic simulations (cf. Fig. 3).

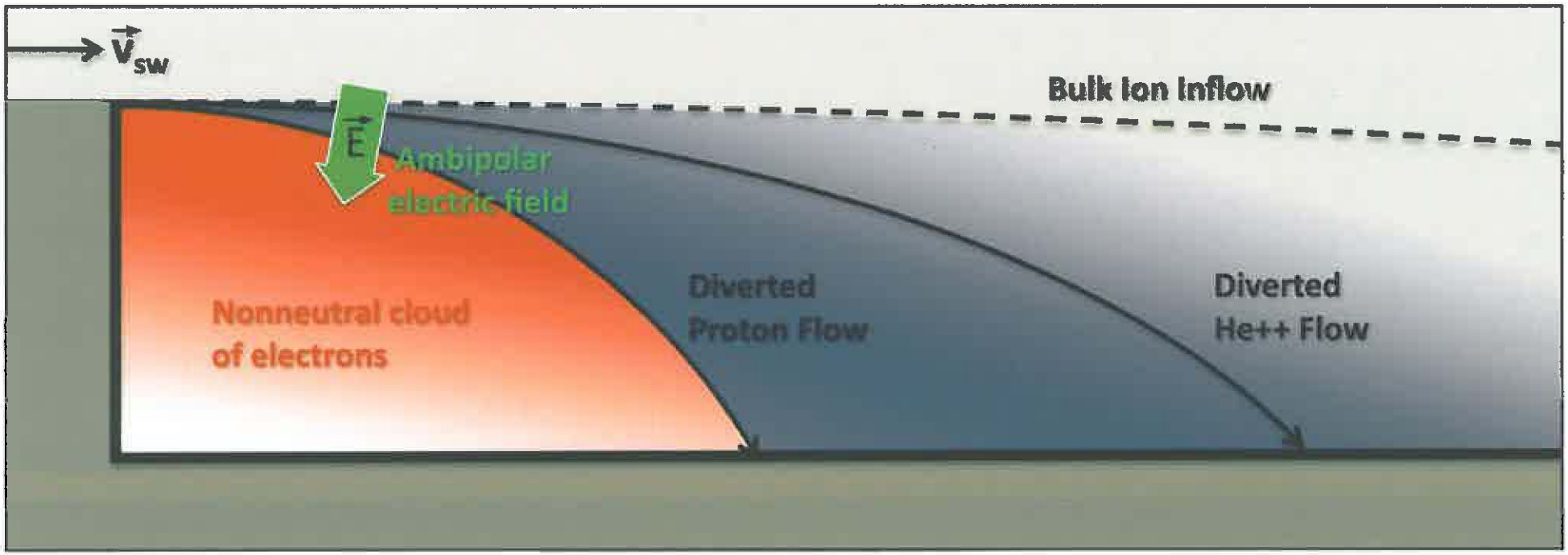
$\vec{V}_{SW}$
Bulk Ion Inflow
$\vec{E}$
Ambipolar
electric field
Nonneutral cloud
of electrons
Diverted
Proton Flow
Diverted
He++ Flow

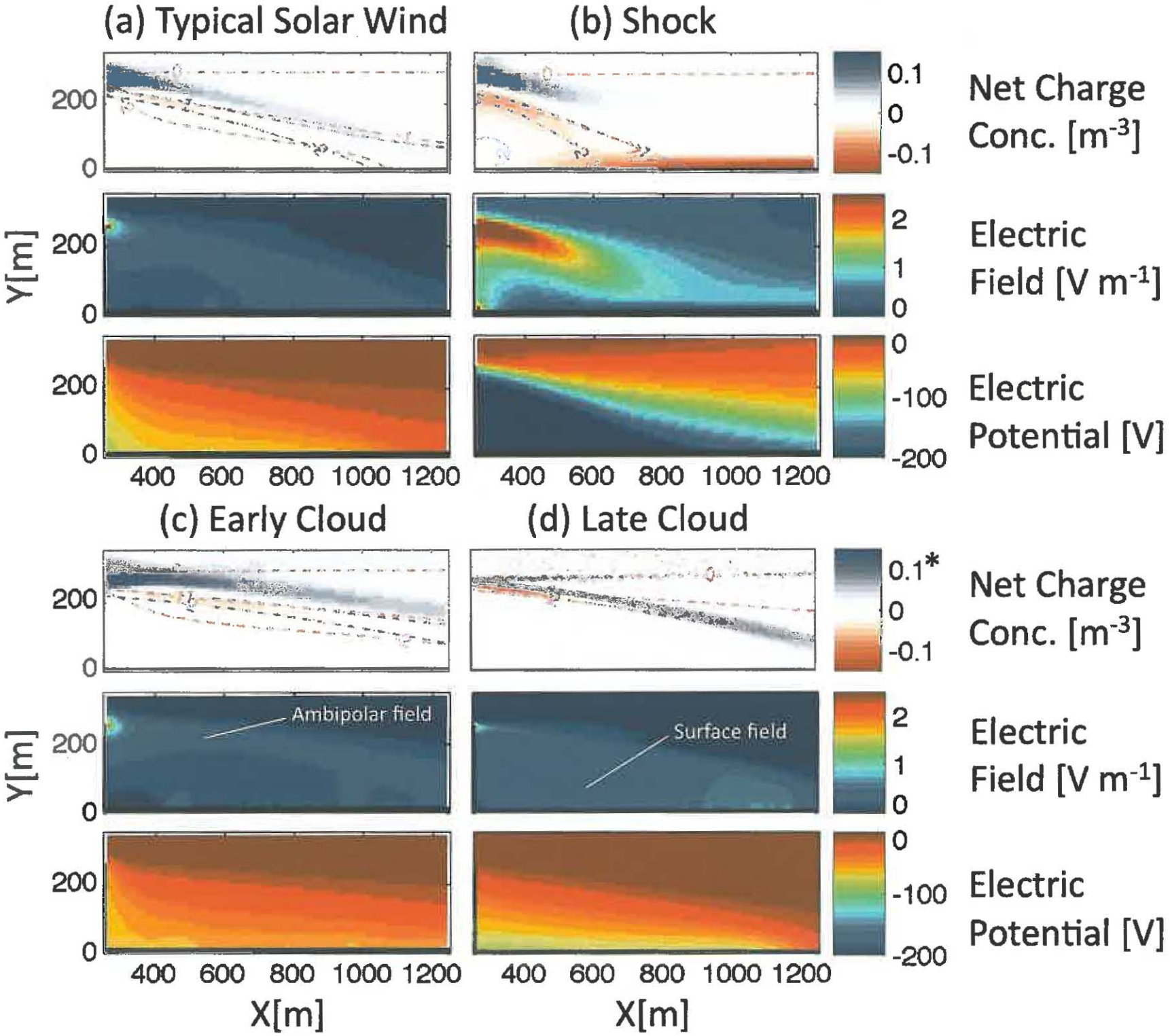
(a) Typical Solar Wind
(b) Shock
(c) Early Cloud
(d) Late Cloud
Y[m]
X[m]
200
0
400 600 800 1000 1200
0.1
0
-0.1
Net Charge Conc. [m-3]
2
1
0
Electric Field [V m-1]
0
-100
-200
Electric Potential [V]
0.1*
Ambipolar field
Surface field

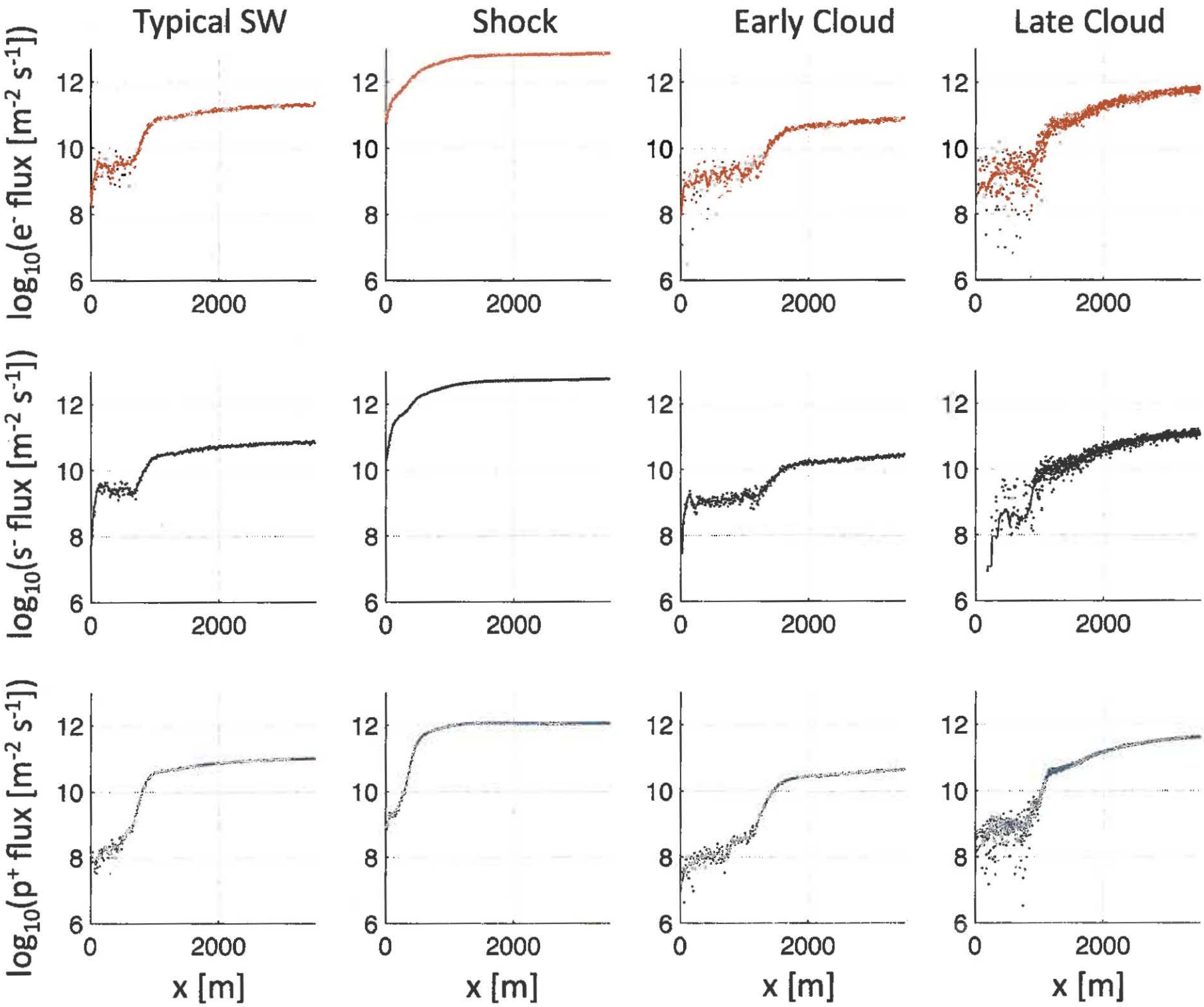
Typical SW
Shock
Early Cloud
Late Cloud
log10(e- flux [m-2 s-1])
log10(s- flux [m-2 s-1])
log10(p+ flux [m-2 s-1])
12
10
8
6
0
2000
x [m]

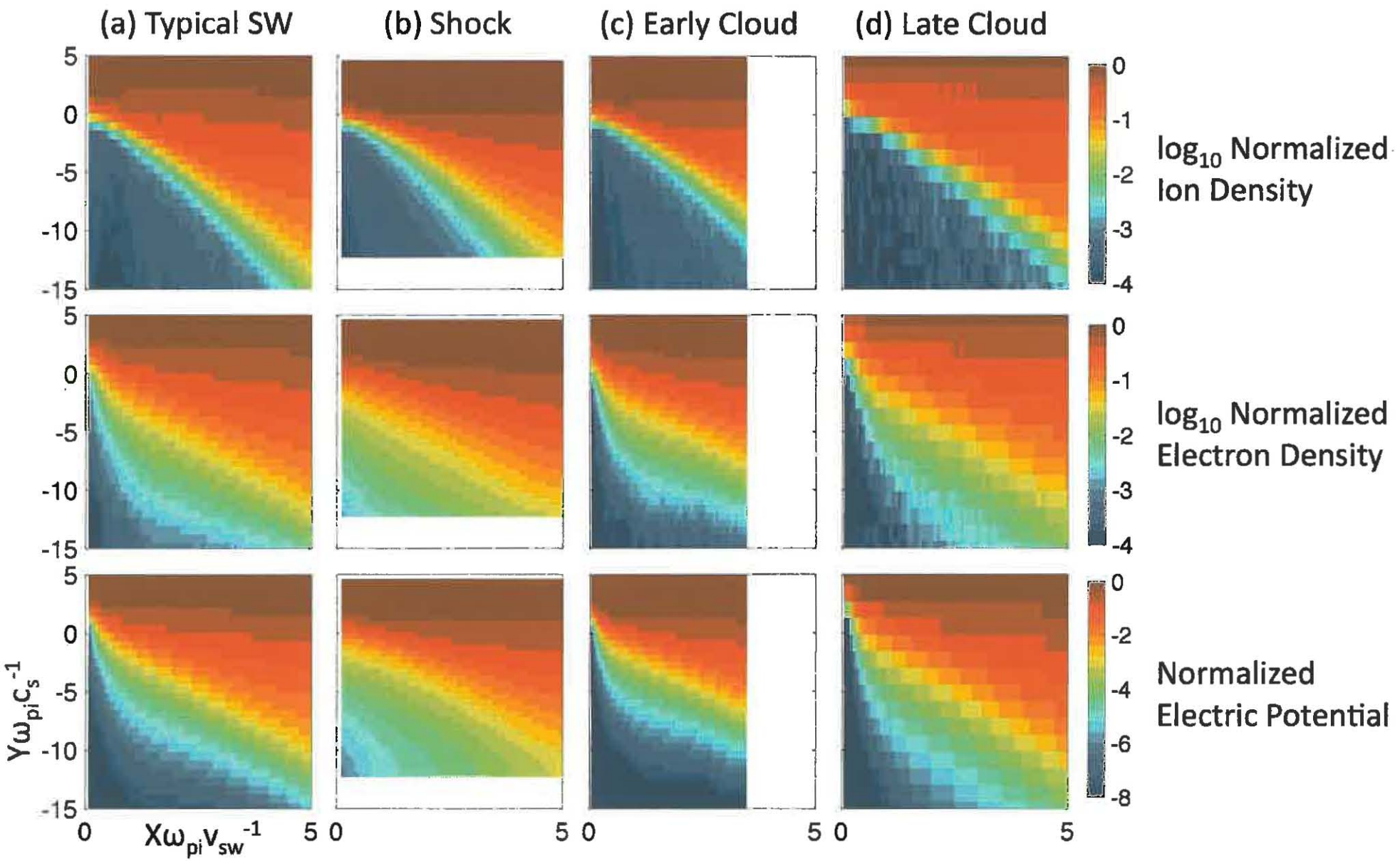
(a) Typical SW
(b) Shock
(c) Early Cloud
(d) Late Cloud
5
0
-5
-10
-15
0
5
$Y\omega_{pi}c_s^{-1}$
$X\omega_{pi}v_{sw}^{-1}$
0
-1
-2
-3
-4
-6
-8
$\log_{10}$ Normalized Ion Density
$\log_{10}$ Normalized Electron Density
Normalized Electric Potential

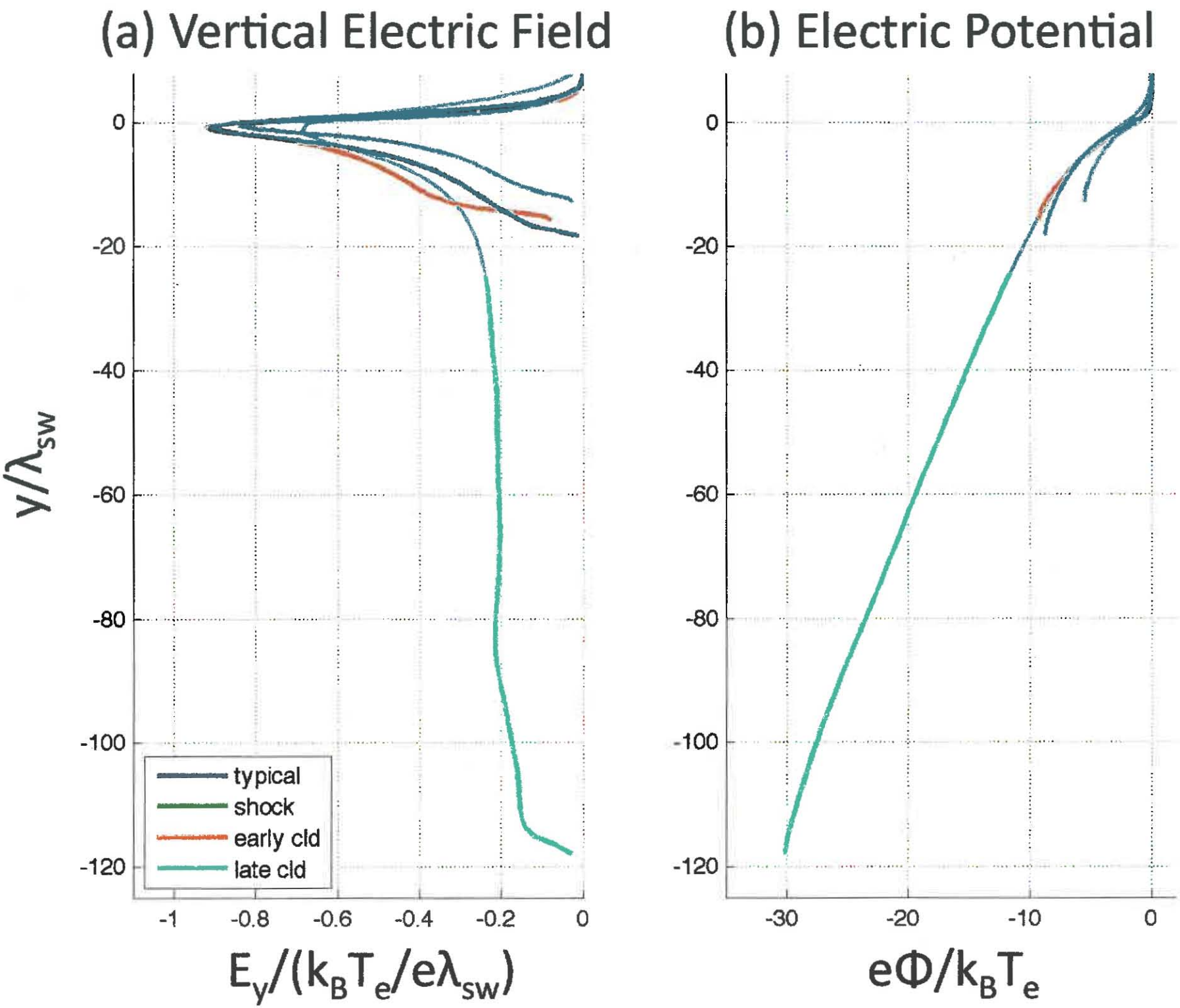
(a) Vertical Electric Field
(b) Electric Potential
y/λsw
0
-20
-40
-60
-80
-100
-120
typical
shock
early cld
late cld
-1
-0.8
-0.6
-0.4
-0.2
0
Ey/(kBTe/eλsw)
-30
-20
-10
0
eΦ/kBTe

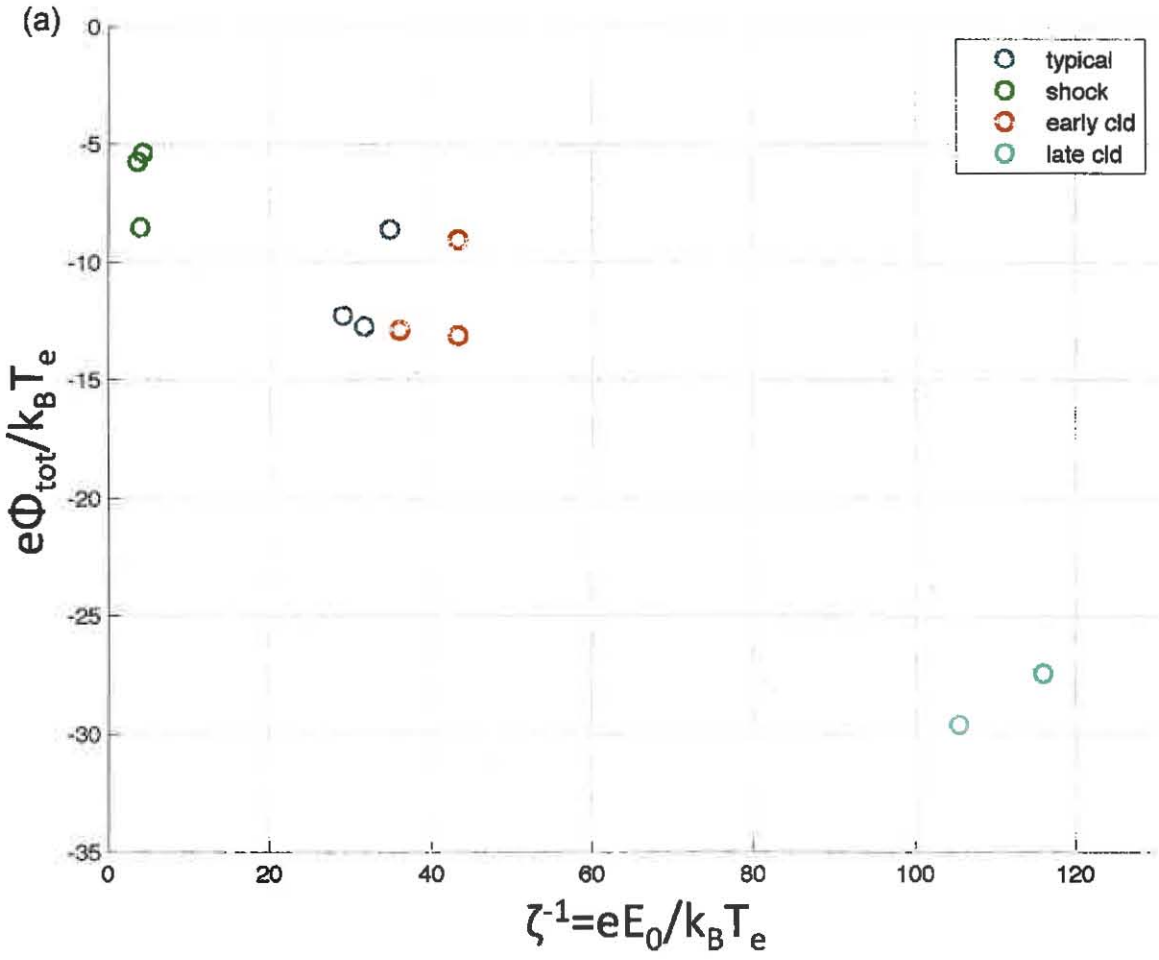
(a)
typical
shock
early cld
late cld
$e\Phi_{tot}/k_BT_e$
$\zeta^{-1}=eE_0/k_BT_e$
0
-5
-10
-15
-20
-25
-30
-35
0
20
40
60
80
100
120

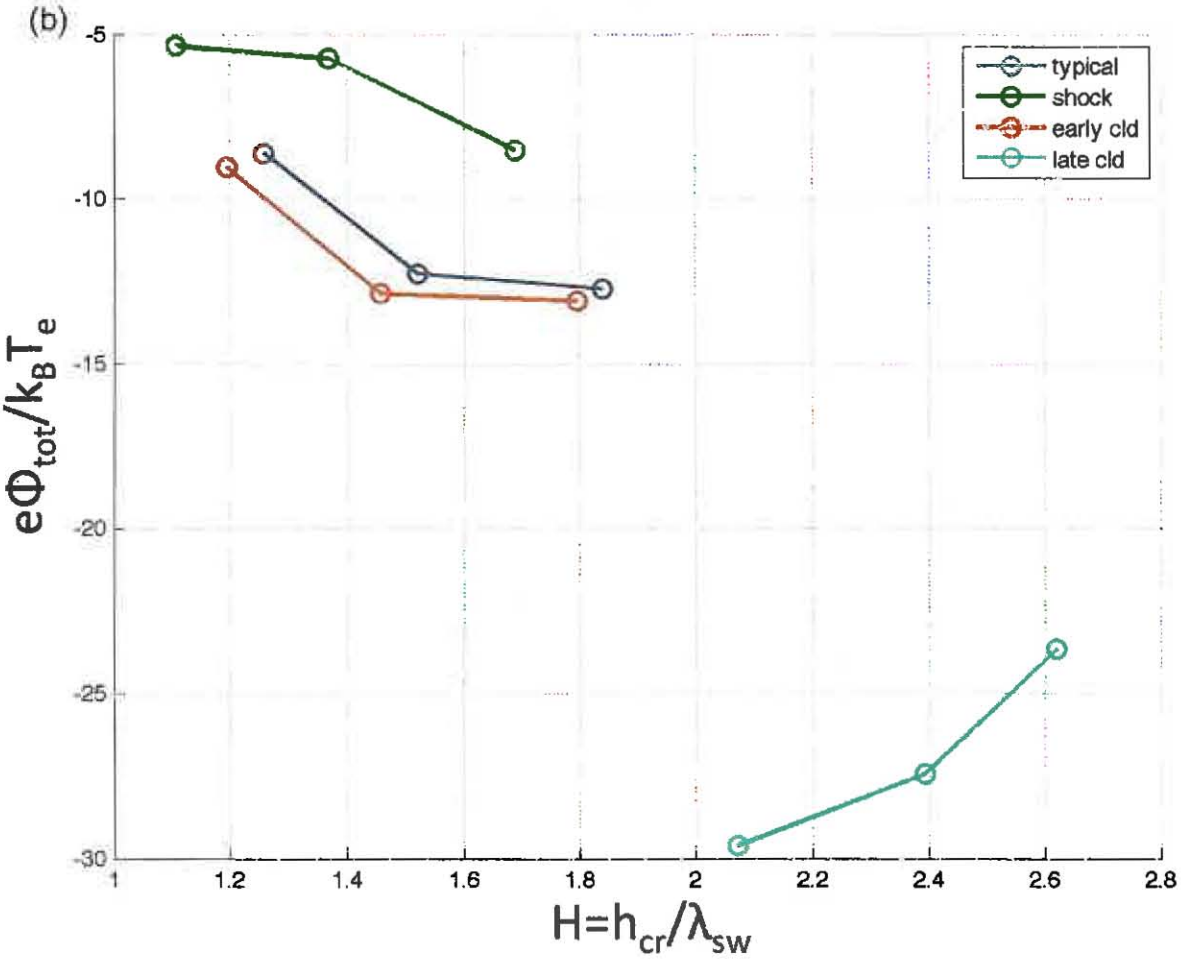
(b)
typical
shock
early cld
late cld
$e\Phi_{tot}/k_BT_e$
$H=h_{cr}/\lambda_{sw}$
-5
-10
-15
-20
-25
-30
1
1.2
1.4
1.6
1.8
2
2.2
2.4
2.6
2.8

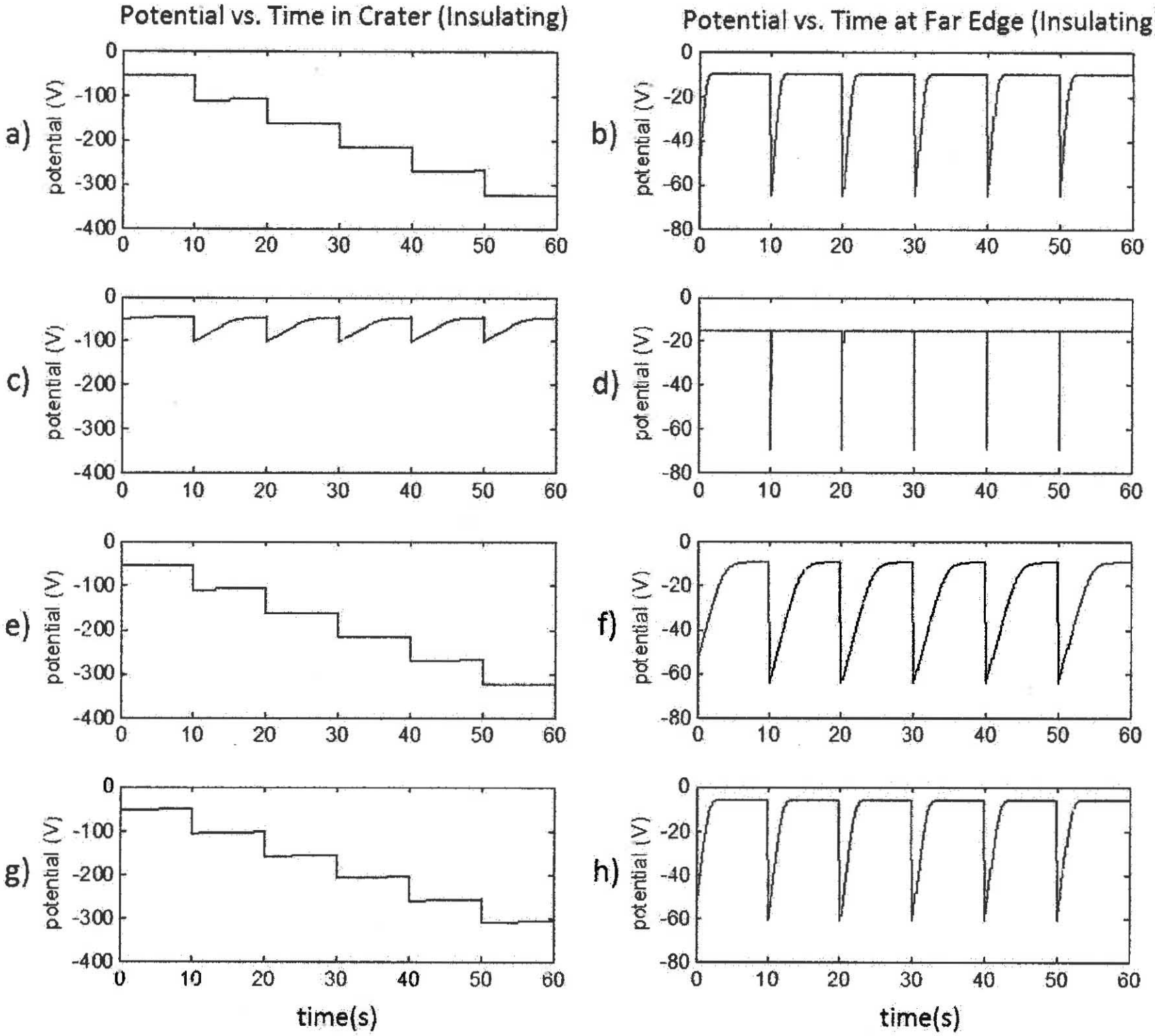
Potential vs. Time in Crater (Insulating)
Potential vs. Time at Far Edge (Insulating)
a)
b)
c)
d)
e)
f)
g)
h)
potential (V)
0
-100
-200
-300
-400
-20
-40
-60
-80
0
10
20
30
40
50
60
time(s)